Electrochimica Acta 391 (2021) 138889

Contents lists available at ScienceDirect

Electrochimica Acta

journal homepage: www.elsevier.com/locate/electacta

CO_2 electro-reduction on Cu_3P: Role of Cu(I) oxidation state and surface facet structure in C_1-formate production and H_2 selectivity

Anders B. Laursen[a,1], Karin U.D. Calvinho[a,1], Timothy A. Goetjen[a], Kyra M.K. Yap[a], Shinjae Hwang[a], Hongbin Yang[a], Eric Garfunkel[a], G. Charles Dismukes[a,b,*]

[a] Department of Chemistry and Chemical Biology, Rutgers, the State University of New Jersey, 123 Bevier Road, Piscataway NJ 08854, United States
[b] Waksman Institute, Rutgers, the State University of New Jersey, 190 Frelinghuysen Road, Piscataway NJ 08854, United States

A R T I C L E I N F O

Article history:
Received 16 November 2020
Revised 2 July 2021
Accepted 4 July 2021
Available online 11 July 2021

Keywords:
Carbon dioxide
Energy storage
Catalysis
Electrochemistry
Carbon utilization

A B S T R A C T

We report the catalytic activity and mechanism of copper(I) phosphide, Cu_3P, with predominant [00I] facet exposure for the electrochemical reduction of CO_2 (CO_2RR) to formic acid. Crystalline nanosheets of this compound that show a preferential [00I] facet orientation exhibit undiminished CO_2RR activity after 16 hours with full retention of crystal structure and surface chemical speciation and no detectable corrosion. In contrast to the range of products formed on Cu metal, CuO, and Cu_2O, the CO_2RR on Cu_3P [00I] produces mainly hydrogen and formate as the sole carbon product in $KHCO_3$ electrolyte. Analysis of the Cu_3P [00I] facet by HAADF-STEM was used to determine the surface lattice structure, while both XPS and Auger spectroscopies were used to determine the surface chemical speciation from the kinetic energies of ionized electrons. The presented analysis identifies isolated trigonal CuP_3 sites on the Cu_3P[00I]-Cu_3P_3 terminated surface and the Cu(I) oxidation state as precursor to the active catalyst. The CO_2RR selectivity to formate and the higher turnover rate for H_2 production on the [00I] facet allows a structure-activity analysis and chemical mechanism to be proposed. Formation of a surface hydride at isolated *H-CuP_3 sites is proposed as the catalytic site in forming both H_2 and formate, while the long Cu—Cu separation retards forming C-C coupling products. These results disprove previously published claims of Cu(I) oxidation state as a sufficient criterion to promote CO_2RR to C_{2+} products, show that stronger bonded hydrides, *H-CuP_3 on Cu_3P, favor production of the C1 product formate over all other carbon products, and predict that stronger formate binding (bidentate) is needed for CO_2RR currents to compete with H_2 production.

1. Introduction

The electrochemical carbon dioxide reduction reaction (CO_2RR) produces fuels or chemicals from water and CO_2 and is powered by electricity that can be sourced from renewables (solar, wind, etc.). Hence, this reaction is a sustainable process for recycling CO_2 captured from point sources or air and can play a central role in addressing climate change. An added advantage of CO_2RR is that excess electricity from intermittent renewable sources may be stored as chemicals for later reinjection into the grid.

Since Hori's foundational work in the 1980s, [1,2] the development of new CO_2RR catalysts has received considerable attention. Catalysts with high activity and selectivity have been uncovered for generating carbon monoxide (CO) [3–6] and formate ($HCOO^-$), [7–10] but high overpotentials are still required for formaldehyde (CH_2O), [11–13] methane (CH_4), [14,15] and methanol (CH_3OH) [16–19] production. In recent years, major improvements have been made in increasing selectivity and lowering overpotentials for C_{2+} products such as ethanol (C_2H_5OH), [20–23] ethylene(C_2H_4), [24–32] isopropanol (C_3H_7OH), [26,33,34] methylglyoxal ($C_3H_4O_2$), [35] 2,3-furandiol ($C_4H_4O_3$), [35] and hydrocarbons. [36] Nanostructured Cu is the most common electrocatalyst for ethanol and ethylene production, where the mechanism is believed to proceed via a coupling of adsorbed *CO intermediates. [37–39] Oxide-derived copper catalysts have thus far shown the most promise for selectively making C_2 products, with Faradaic efficiencies up to 70%. [15,40,41] The C_2 activity has been attributed to residual Cu(I) species in the Cu metal formed upon reduction. [15] However, the major drawback of these copper-based catalysts is the high overpotential requirement, with corresponding low cathodic energy efficiency (45%). [31]

Distinct from copper metal and its oxides, the formation of C_3 and C_4 products on nickel phosphides has shown significant advantages in terms of Faradaic efficiency (72% for 2,3-furandiol),

* Corresponding author.
E-mail address: dismukes@chem.rutgers.edu (G.C. Dismukes).
[1] These authors contributed equally.

https://doi.org/10.1016/j.electacta.2021.138889
0013-4686/

overpotential (10 mV), and cathodic energy efficiency (>90%), while current densities have lagged behind (<0.5 mA/cm^2). [35] Mechanistically similar to the pathway in natural enzymes [42–44], the C_3-C_4 products form through hydride transfer to CO_2, successively generating *formate then *formaldehyde which polymerizes via enol condensation and dehydrates to methylglyoxal. [35,45] Surface activation of *methylglyoxal generates the enol form, which can add CO_2 forming 2,3-furandiol. [35] A similar mechanism for producing 1-butanol from the polymerization of formaldehyde and further condensation reactions was proposed on CuP_2. [46] In this study, the authors confirmed the absence of CO* intermediates on the surface using *in situ* surface-enhanced infrared absorption spectroscopy, further supporting the above mechanism on transition metal phosphides. [46]

Herein, we report the synthesis, surface structure, electronic structure, and catalytic activity of highly-crystalline single-phase copper(I) phosphide, Cu_3P, with predominant [00l] facet exposure for the electrochemical reduction of CO_2 to formic acid. The copper-phosphorous phase diagram indicates that pure copper forms a single binary compound Cu_3P at increasing P content and temperatures below 700°C. [47] Such simple phase behavior enables the assessment of the oxidation state preference for CO_2RR. We target the formation of a stable and dominant surface facet structure to gain information about the structure-activity relationship in copper compounds. A previous report of polycrystalline Cu_3P as a nanocrystalline catalyst for CO_2RR by Peng et al. [6] showed only the formation of CO, a product not detected in either our work or the recent report by Schaidle et al. [48] The latter report describes a versatile method for the controlled synthesis of phase-pure Cu_3P nanoparticles by thermal decomposition of $[Cu(H)(PPh_3)]_6$ in oleylamine. These authors reported electrochemical studies of this material supported on carbon paper electrodes and found the products are mainly H_2 and some formate at Faradaic efficiencies below 8% (max. at $E = -0.30$ V versus RHE in 0.1 M $KHCO_3$).

Similar to nickel phosphides, Cu_3P can be expected to form surface hydrides in an aqueous solution during reductive polarization. [49] However, unlike Cu_3P, six binary nickel phosphide compounds form at 700°C, and each can form multiple structurally and energetically distinct hydrides. These hydrides may potentially react with water (or protons) to form H_2 or CO_2 to form either formic acid or CO and water or undergo further CO_2RR. What controls the branching between these pathways and turnover frequency (TOF) is the subject of extensive current research. Concepts so far considered in controlling reactivity have been hydricity, [50–52] oxidation state, [15,53] crystal structure, [54] and morphology [22] of these surface species.

2. Results and discussion

2.1. Catalyst preparation

Due to low conductivity, a bulk powder of Cu_3P could not serve as an electrocatalyst at any relevant current density. Instead, to ensure an intrinsic Cu_3P activity was determined, a phase-pure Cu_3P nanostructured film was synthesized on a mechanically polished Cu foil substrate. The resulting uniformly Cu_3P-coated Cu foil electrode was termed Cu_3P NS/Cu. Briefly, catalyst synthesis (see SI for details): Cu foils were mechanically polished, sonicated three times in 1 M HCl, water, and acetone; then air-dried. The reaction vessel was evacuated of O_2, re-filled with N_2 prior to 45 min reaction of the cleaned foils in tri-octylphosphine/tri-octylphosphine oxide (TOP/TOPO) solution under an N_2 flow at 310°C, maintained by immersion in a pre-heated sand bath (ensuring rapid heating to reaction temperature). After air quenching, the foil was sonicated in an acetone/ethanol mixture to remove excess loose Cu_3P product, yielding the final catalyst used in subsequent analyses. It is important to note that the catalyst was stored in a desiccator to avoid excess surface oxidation by moist air.

Cu_3P was etched in 30% NH_4OH before catalytic evaluation to remove the surface oxide formed due to air exposure after electrode synthesis. It was observed that, in the absence of this treatment, the combined HER and CO_2RR Faradaic efficiencies did not reach 100% even after 16-hour reactions at the highest reductive potentials (-0.5 V vs. RHE) (see Fig. S1). No additional gas or liquid products could be detected. The less than stoichiometric Faradaic yield indicates that significant charge could be directed to Cu-phosphor-oxide reduction in the absence of the pre–catalysis etch. The re-reduction of the surface oxide back to Cu_3P is similar to what is observed for cobalt phosphate in the literature. [55] In contrast to Cu_3P, Cu_2O is seen to reduce in part to Cu even under the relatively small applied overpotentials investigated here (vide infra) in agreement with literature reports. [22]

The synthesized catalyst on Cu foil (Cu_3P NS/Cu) was masked to ensure only the front foil surface was exposed. A flourosilicone polymer gasket and HDPE mask were fabricated to protect the electrical back-contact area and accurately select the exposed geometric electrode area. The activity of Cu_3P NS/Cu was benchmarked to Cu foil, prepared as described in literature [56], and Cu_2O thin film on Cu foil (Cu_2O/Cu), formed by thermal oxidation of Cu foils modified from ref [57], annealed at 500°C for 6 hr in air.

2.2. Catalyst bulk characterization pre- and post-catalysis

Characterization tools description and sample preparation is shown in SI. PXRD was used to determine the bulk crystalline structure of Cu_3P NS/Cu (Fig. 1A and B show the PXRD pattern and crystal structure, respectively). Pristine Cu_2O/Cu was shown to be a mixture of Cu_2O, CuO, Cu_8O, and Cu by PXRD (see Figs. S2–S4), and electropolished Cu foil shows only the presence of metallic Cu with some anisotropy in the grain-size, as is common in rolled metal foils. SEM analysis was used to investigate the morphology of the three investigated catalysts (see SI for details on post-catalysis prep). The morphology of pristine Cu_3P NS/Cu was observed to consist of nanosheets extending vertically up from the Cu foil (z-axis) with the normal to the sheets oriented randomly in the xy-plane (see Fig. 1C). Individual sheets were mainly 0.2 - 0.5 μm in thickness and 1-8 μm in width and length, with some smaller hexagonal sheets observed (100-500 nm and < 30 nm in thickness, see Figs. S5–S6). From the cross-section analysis in Fig. 1C, the film thickness is seen to be 10-30 μm and uniformly porous throughout. The porosity should provide electrolyte penetration throughout the film. SEM images of the benchmark Cu_2O/Cu film show very small pores, hardly resolved by the SEM in the cross-section view (Fig. 1C) < 1 μm and corroborated in literature. [57] The electropolished Cu-foil is smooth within the resolution of the SEM. Some Cu-grain-boundaries may be resolved as slight differences in contrast by the back-scatter detector. All three samples show that the morphology is retained after electrolysis.

The HRTEM HAADF image in Fig. 1D shows the hexagonal nanosheet structure with two sheets next to each other (see also low magnification HAADF STEM in Fig. S5). STEM EELS mapping of this site shows the Cu and P sheets with a thin phosphor-oxide layer, 3.4 ± 0.9 nm, seen as a higher oxygen concentration (deep blue color). HAADF STEM images show this layer is disordered; see Fig. S6. Fig. 1E shows the HR-STEM HAADF image of a Cu_3P nanosheet along the [00l] zone axis with atomic resolution. The crystal structure overlay verifies that the Cu_3P[00l] facet is the primary surface facet exposed to the electrolyte. We note that the facet exposure differs from that reported by Han et al., likely due to the different synthesis methods. [58]

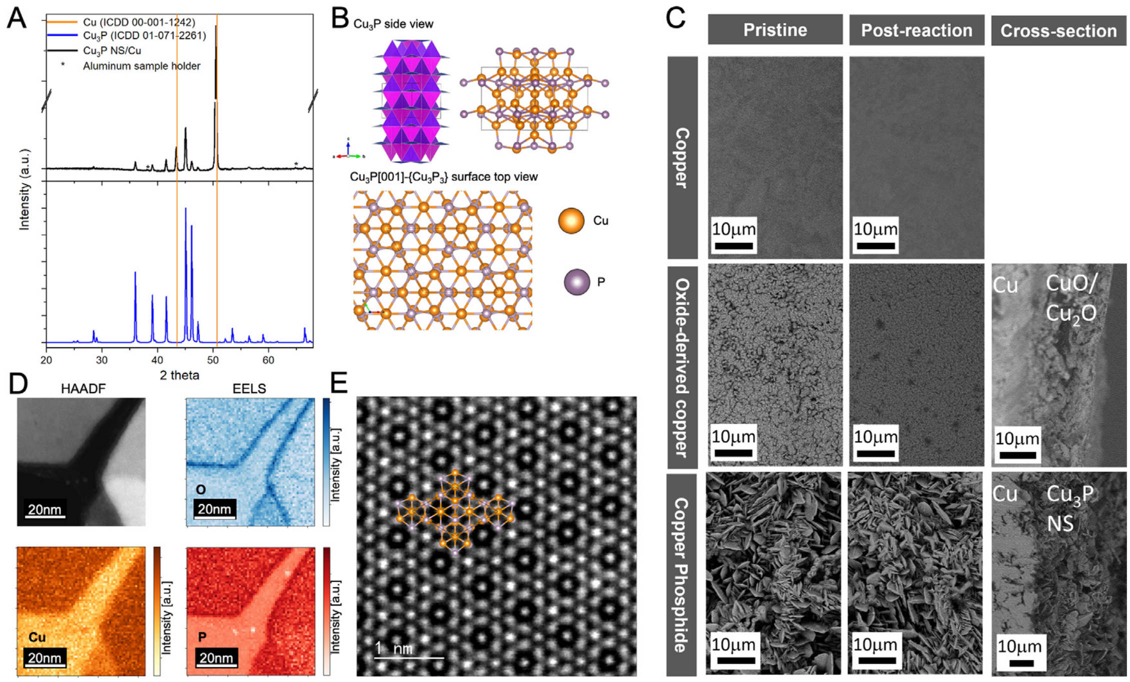

Fig. 1. (A): PXRD pattern of as-synthesized Cu_3P NS/Cu and reference pattern ICDD 01-071-2261. (B): Crystal structure of reference Cu_3P, side-view, and top-view. (C): SEM images of the Cu, Cu_2O/Cu, and Cu_3P NS/Cu surface before and after CO_2RR, as well as cross-section SEM images of porous Cu_2O/Cu and Cu_3P NS/Cu as thin films on Cu foil. (D): HAADF-STEM image of pristine Cu_3P NS, EELS map of Cu L-edge (orange), P L-edge (red), and O K-edge (blue), respectively. (E): High-resolution HAADF image of a Cu_3P NS along its [00l]-zone axis with the structure model overlaid on top, providing evidence of the exposure of the Cu_3P[00l] facets. (For interpretation of the references to color in this figure legend, the reader is referred to the web version of this article.).

2.3. Electrochemical activity

Fig. 2A compares the linear sweep voltammetry (LSV) of the Cu_3P NS/Cu in CO_2-saturated 0.1M $KHCO_3$ electrolyte (pH 6.8) to Ar-saturated 0.1 M phosphate buffer (pH 6.8). The cathodic current is suppressed at potentials negative of -0.7 V vs. RHE in the presence of CO_2, indicating that CO_2 suppresses the HER activity. At applied potentials positive of this potential, the current is the same within experimental uncertainty. The latter behavior differs from that on various Ni_xP_y compounds (x/y = 12/5, 2/1, 5/4, 1/2) where CO_2 reduction contributes an increasing fraction to the total current as potentials more positive than -0.7 V vs. RHE are applied. [35] Accordingly, a larger overpotential is needed before CO_2 electroreduction on Cu_3P can contribute appreciably to reaction current relative to HER. We note that the open-circuit potential for the Cu_3P NS/Cu catalyst immediately after electroreduction is about -0.1 V vs. RHE. The open-circuit potential indicates the limiting potential for the electrocatalyst to remain in its reduced state, since at any potential more positive of this value electro-oxidation of the catalyst (or formed products) would occur. Therefore, the effective region for CO_2RR is between -0.1 and -0.5 V vs. RHE.

The Faradaic Efficiency (FE) for the observed formic acid (FA) product is shown in Fig. 2B for Cu_3P NS/Cu, Cu_2O/Cu, and Cu. It is seen that the FE on Cu_3P NS/Cu is nearly constant throughout the potential range (FE = 1.1 % ± 0.6 %) with a minor increase negative of -0.3 V (1.8 % FE). By contrast, FE increases with applied potential for the two benchmark materials. Furthermore, it may be seen that Cu_3P NS/Cu makes only formic acid in the entire potential region. Fig. S1 in the SI shows that the residual current density is used to form hydrogen, H_2. We note error bars are shown on all Cu_3P NS/Cu FE measurements. However, the error is too small to be seen at low applied potentials and increases with the H_2 current, likely due to H_2 bubbles blocking CO_2 access to the catalyst surface.

The turnover frequency (TOF) for the two-electron transfer (equivalent to a hydride transfer) to either hydrogen or formic acid production was calculated for Cu_3P NS/Cu and the two benchmark Cu-catalysts using their electrochemical surface areas (see SI for details). It should be noted that this method relies on the specific capacitance for each transition metal phosphide/oxide/metal, which is unknown, and so a common literature approximation is used here to allow direct comparison to other studies. [59–61] The TOF has the advantage of normalizing to the true surface area when comparing nanoporous Cu_2O/Cu or Cu_3P NS/Cu to flat Cu catalysts. Since the hydrogen species on nickel phosphides are best described as a hydride (H^-) species (partial negative charge on H), [61,62] we adopt a similar description for Cu_3P NS/Cu. This description posits that a surface hydride may either react with CO_2 to form formic acid (formate + H^+) or with water (or protons depending on pH) to form H_2 (see further discussion of this assumption below). Hence, hydride TOF is a good descriptor for the combined activity for both HER and CO_2RR. Fig. 2C shows that the total TOF (H_2 + CO_2RR) for Cu_3P NS/Cu is higher at all potentials than the Cu-based references. However, as stated above, the FE for CO_2RR is low and produces only formic acid. Hence, we show the formic acid TOF in Fig. 2D. From this, it may be seen that at all potentials, the low FE to formic acid on Cu_3P NS/Cu is actually caused by competition with a very high TOF for HER. In fact, the Cu_3P NS/Cu is on par with the formic acid TOF on both benchmark catalysts across all potentials. Comparing the two benchmark catalysts, it is seen that at low overpotentials, Cu_2O produces a higher TOF to formic acid over the Cu-benchmark catalysts, but at more negative potentials where HER wins, the Cu foil catalyst produces more formic acid than Cu_2O/Cu. This outcome agrees with literature reports of an earlier onset for CO_2RR on Cu_2O compared to on Cu. [1,57] Cu_3P NS/Cu thus serves as a more selective catalyst for formic acid production across a wider potential range than either of the benchmark catalysts, though its low FE is still unsuitable for application in CO_2RRs. It should further be noted that the competition between hydride species reacting with proton/water or CO_2 can be tuned in a variety of ways including changing the nature of the hydride bonding with periodic trends arising from differences

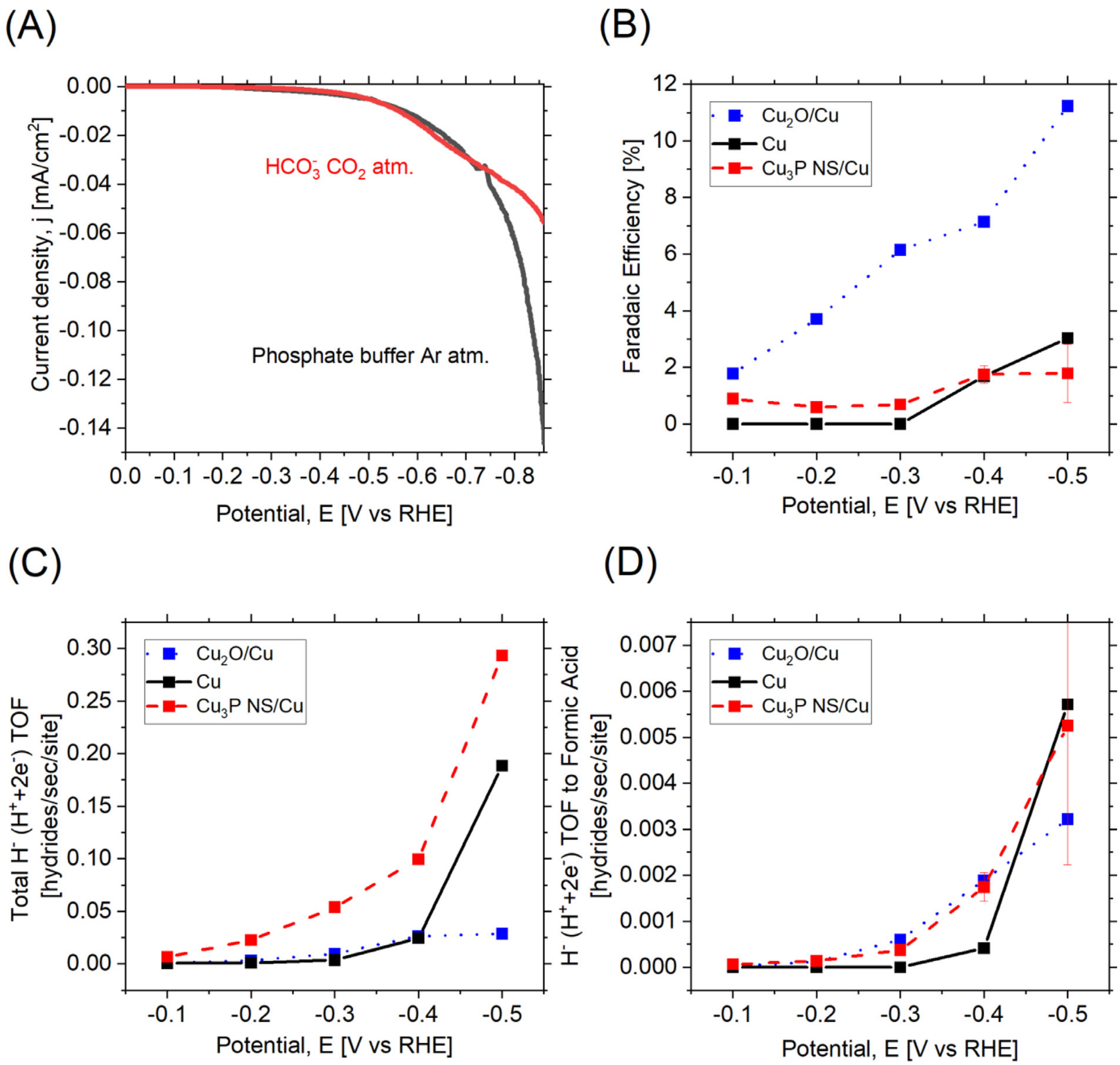

Fig. 2. (A): Linear sweep voltammetry (scan rate: 10 mV/s) of Cu_3P in 0.1 M $KHCO_3(aq)$ under CO_2 and phosphate buffer under Ar. (B): Formic acid Faradaic efficiency on Cu_3P. (C): Total hydride turnover-frequency (TOF to H_2 + CO_2RR) per site vs. applied potential for Cu_3P/NS/Cu, Cu_2O/Cu, and Cu. (D): Formic Acid TOF per site vs. potential.

in orbital energies and overlap between the hydrogenic 1s, 2s and 2p bonding sets and the molecular orbitals of the bonded surface atom. Other strategies explored in the scientific literature is to tune the electrolyte pH where lower values favors HER due to the abundance of protons, while at high pH water dissociation lowers HER activity due to lower availability of free water molecules and their lower chemical potential in response to electrostriction (activity correction). [63] Another approach was described in our previous work with nickel phosphide compounds, where we demonstrated that by reducing the applied potential the HER can be thermodynamically limited relative to thermodynamically more favorable CO_2RR reactions. [35] However, complex multi-step CO_2RR reactions are kinetically disfavored over single-step HER. Other possible strategies could involve reducing the water access to the active site or by use of hydrophobic surroundings, as Nature does in many enzymes.

2.4. Comparison to electrocatalysis literature

Since very few CO_2RR studies report the TOF, we may only compare the FE at optimized potentials summarized in Table 1 above. Here we consider "optimal" as the highest FE at the lowest possible overpotential, ensuring the highest energy efficiency of the reaction. While this is not the only requirement for a viable process, it is an important first criterion. Firstly, we note that the thermodynamic limiting potential for formic acid synthesis is reported as non-linearly dependent on pH, with a change from Nernstian behavior below the pKa ~ 4 of formic acid, while above this pH it is -0.035 V vs. RHE. [39] Hence, the maximal FE to formic acid on Cu_3P NS/Cu we observe is 0.9% at -0.1 V vs RHE (η = 65 mV) or ~1.8% at potentials between -0.4 and -0.5 V vs RHE (η > 365 mV). This optimal potential range is in excellent agreement with that observed for polycrystalline Cu_3P/Carbon. [48] For comparison, CuO_2/CuO/CuS has shown the largest selectivity for formic acid for a Cu-based catalyst at 84% FE at -0.7 V vs. RHE [65] (η = 665 mV) in 0.5 M $KHCO_3$. The authors did not investigate the FE vs. potential dependence for the CuO_2/CuO/CuS catalyst, thus precluding comparison at the same overpotential. Other state-of-the-art formic catalysts are nanostructured SnO_2 [66] or Pd-Pt alloy on carbon, [64] with a FE of 8% at -0.36 V vs RHE (η = 325 mV) and 88% at -0.4 V vs RHE (η = 365 mV), respectively. The 8% FE result is in close agreement with the recent study of Cu_3P/carbon

Table 1
Comparison of Faradic efficiencies and overpotentials for various literature CO_2RR to formate catalysts.

Catalyst	Faradaic Efficiency [%] Formate/Formic acid	Overpotential [mV]	Reference
Cu_3P NS/Cu	0.9	65	This work
Pd-Pt-alloy/C	88	365	[64]
CuO_2/CuO/CuS	84	665	[65]
Cu_3P/C NP	8	265	[48]
Nanostructured SnO_2	8	325	[66]
Cu_3P/C	0	N/A	[6]

nanoparticles by Schaidle et al. [48] and contrasts to Peng et al., who observed only CO as carbon product and no formate. [6] These authors did not perform post-reaction characterization, nor did they consider removing the air-exposed surface oxide, which we show herein changes the FE and could potentially influence the C/H selectivity if Cu enrichment occurs. Thus, while Cu_3P NS/Cu is not the most selective catalyst for formic acid, it exhibits activity at the lowest applied potentials reported for a non-platinum group metal catalyst. This provides systematic trends for comparison to other transition metal phosphides and is important for understanding the fundamental chemical mechanism of this class of electrocatalysts.

2.5. Surface post-catalysis characterization

In order to understand the mechanism of catalysis, we examined the surface chemical species on Cu_3P NS/Cu, Cu_2O/Cu, and Cu by measuring the kinetic energy of ionized electrons using XPS spectroscopy and additionally analyzing the Auger excitations, Fig. 3A–C. The Cu 2p XPS spectra show only small binding energy shifts between the different phases (see Fig. S 10). According to the NIST XPS database and other reference data, Cu $2p_{3/2}$ signals for Cu and Cu_2O are overlapping [67,68]: Cu (932.50–933.10 eV), and Cu_2O (932.20–932.80 eV). There are no tabulated XPS references for Cu_3P in the NIST database.[68] The only tabulated values are for CuP_2 (Cu $2p_{3/2}$ 932.2-932.4 eV), placing it in the center of the Cu^0-Cu^{I+} range. This agrees with the observed behavior of nickel phosphides, which show a partial charge on Ni $\delta <$ I+. [35,60,61] Instead, Cu^0 and Cu^{1+} may be differentiated by the latter having a broader peak (larger FWHM) and a weak satellite doublet peak starting at 945 eV. Unlike these, CuO is identified by a doublet with a $2p_{3/2}$ peak position at (932.90–934.60 eV) and a strong satellite doublet peak feature at 943 eV.

Additionally, the Cu Auger LMM lines show a fingerprint of the surface electronic state. Hence we can rely on a combination of these two techniques to determine the surface speciation. Starting with the simplest case, Fig. 3C shows the CuLMM Auger peaks of pristine Cu (post-sputtering) with the characteristic kinetic energy peak position for metallic Cu (918.6 eV) and three well-defined satellites, two at lower and one at higher kinetic energy. [67] The XPS spectrum (see Figure S10) shows a single doublet with the Cu $2p_{3/2}$ peak position at 932.4 eV and an FWHM ~1.5 eV, corresponding to Cu^0. After extended electrocatalytic reaction, the kinetic energy of the Auger peak decreases to 918.3 eV (Fig. 3C) between the values for Cu and CuO; [67] in addition, the peak shape broadens. The spectra can best be interpreted as the superposition of oxidation states with Cu^0 as the dominant species. The XPS (see Fig. S10) shows two doublet peaks with the Cu $2p_{3/2}$ peak positions at 932.7 and 934.7 eV, respectively - with the latter having a much smaller intensity. From this, we assign the latter peak to CuO. The former peak position could be attributed to either Cu $2p_{3/2}$ from Cu and/or Cu_2O. However, as state above, the Auger LMM line position indicates the dominant species is Cu^0. The XPS Cu $2p_{3/2}$ peak is slightly broadened compared to before catalysis with an FWHM of 1.9 and shows a very weak satellite feature around 945 eV (see Fig. S10), indicating small amounts of Cu_2O. Hence, post catalysis, the Cu-foil shows all degrees of oxidation: Cu, Cu_2O, and CuO. Some of these oxidized species could originate from the air exposure between the end of the reaction and analysis. Fig. 3B shows the Auger spectrum of pristine Cu_2O/Cu with a broad, intense satellite at kinetic energies from 916–909 eV and a peak position of 917.8 eV. Comparing this to the NIST database, [68] This is indicative of a CuO-dominated surface. The detailed XPS analysis (see Fig. S10) shows a doublet with a Cu $2p_{3/2}$ peak binding energy at 934.8 eV and two strong Cu^{2+} satellite features at 931 and 943.5 eV, all indicating a significant fraction of CuO. A second doublet with a Cu $2p_{3/2}$ at 933.4 eV is indicative of a deshielded (oxidized) Cu species with an FWHM of ~2 eV, indicating a Cu_2O species. After electrolysis, the Auger LMM peaks indicate two major species based on peak positions, a strong Cu_2O peak at 915.6 eV and a Cu shoulder peak at 918.1 eV. Detailed XPS analysis (see Fig. S10) confirms the absence of CuO (no strong satellite around 931 eV and 944 eV), the absence of the doublet for Cu $2p_{3/2}$ at ~934.7 eV, but has one doublet for a Cu 2p3/2 peak position at 932.7 eV instead. The presence of two weak satellite features at 945.1 eV and 946.9 eV confirms the presence of Cu_2O, also seen in the Auger LMM spectra. The relatively narrow FWHM of 1.4 eV for this peak confirms a Cu^0 chemical species.

In summary, the pristine Cu_2O/Cu catalyst is best assigned as a surface Cu^{2+} oxide on a Cu^{1+} oxide with the Cu substrate below the detection depth by XPS and Auger, but detected by PXRD as stated above. We denote this surface as CuO/Cu_2O/Cu. After electroreduction, the XPS and Auger analysis indicates Cu_2O and likely a small amount of Cu^0. This suggests that at the reducing reaction conditions, the CuO is unstable concerning reduction to Cu_2O. The small amount of Cu^0 that appears could indicate that the Cu_2O will eventually reduce fully to Cu, but that the kinetics of this is relatively slow. [22]

Fig. 3C shows the Auger LMM spectrum for pristine Cu_3P NS/Cu) with a peak position of 917.4 eV, a satellite peak at 919.9 eV, and 915.5 eV. These peaks are not attributable to CuO, Cu_2O, nor Cu^0 but rather are unique to the Cu_3P phase. Analysis of the Cu XPS in Fig. 3D shows a single doublet with a Cu $2p_{3/2}$ peak position at 932.9 eV slightly deshielded from that of Cu^0 (932.4 eV, see above) close to that seen for Cu_2O above (932.7 eV). The presence of two weak satellites at 944.7 eV and 948 eV are fairly close to the expected values for Cu_2O (945.1 eV and 946.9 eV above) while still slightly shifted. After catalysis, the same XPS (Fig. 3E) and Auger LMM (Fig. 3A) spectra are seen with the main peak positions conserved within 0.1 eV error, indicating a surface chemical stability of the catalyst.

In summary, Cu_3P retains its electronic structure after electrolysis (from analysis of both XPS and Auger peaks) and its bulk composition and structural phase (by PXRD). As no bulk phase change is observed experimentally, we can preclude any change in the oxidation state of the bulk phase. The XPS analysis indicates that Cu in Cu_3P is close to that of a formal Cu^{I+} oxidation state but slightly more deshielded, consistent with relatively greater Cu→P electron transfer in Cu_3P compared to Cu_2O, as expected based on elementary concepts in covalent bonding (increased Cu-P orbital

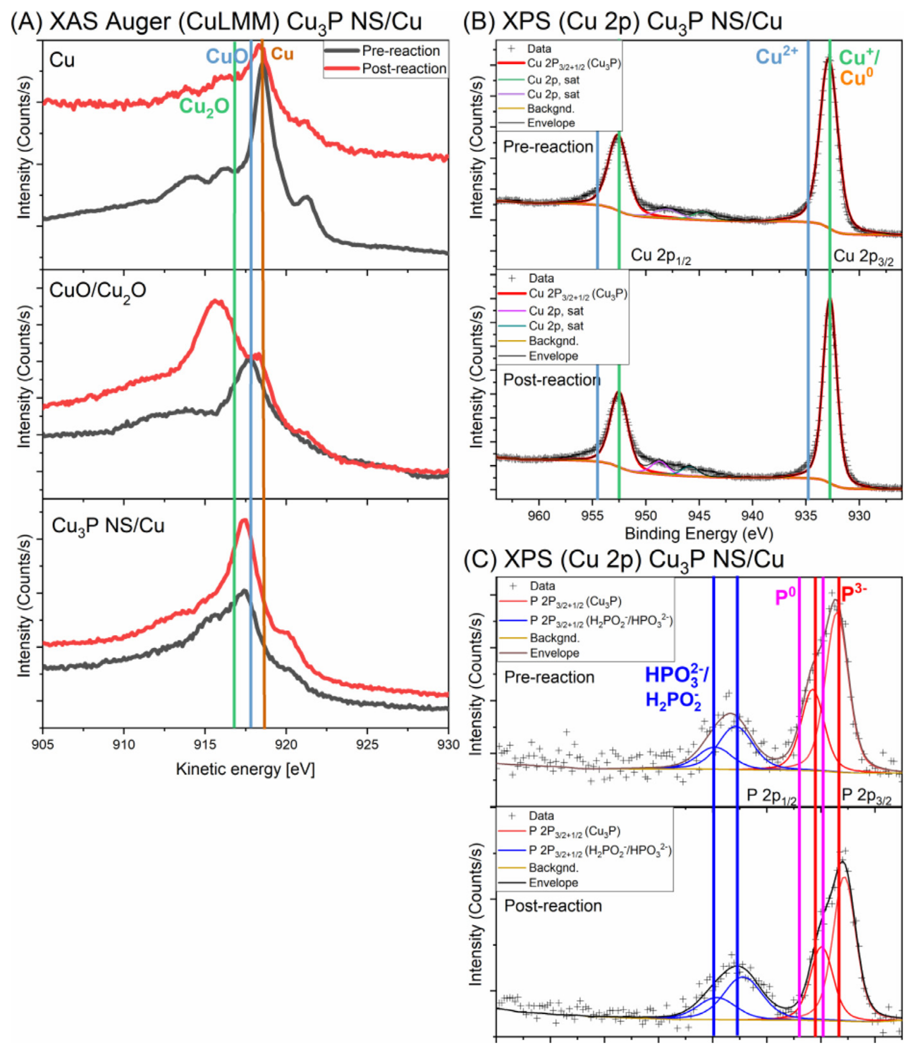

Fig. 3. (A) LMM Auger spectra of (from the top) Cu, Cu_2O/Cu, and Cu_3P NS/Cu before and after catalysis. (B) shows the XPS detailed analysis and fitting of the Cu 2p binding region of Cu_3P NS/Cu pristine (top) and post-catalysis (bottom), respectively. (C) shows the P 2p binding region of Cu_3P NS/Cu pristine (top) and post-catalysis (bottom), respectively.

overlap and smaller valence Cu(3d)-P(3p) atomic energy gap). This increased covalent bond order is likely also the reason for the improved stability over Cu_2O, which showed a tendency towards reduction to Cu^0.

Finally, we examined the P $2p_{3/2}$ and $2p_{1/2}$ doublet region, which we attribute (based on peak positions) to the transition metal phosphide and surface oxide (see Fig. 3D and E). We observed no significant difference between the spectra before and after catalysis. Both samples show a P $2p_{3/2}$-peak at low binding energy (P $2p_{3/2}$ = 129.4 eV and 129.1 eV, before and after catalysis respectively), attributable to the transition metal phosphide (P $2p_{3/2}$ = 129.4 eV for compositional analog Ni_3P (although not a structural analog) and 130 eV for P^0). [68] The slight reduction in binding energy after catalysis indicates an overall slight reduction of the surface P-species post-catalysis, attributable to some additional P→Cu electron transfer. Both samples also show a doublet at high binding energy with a $P2p_{3/2}$ peak position at 133.1 and 132.9 eV, respectively. By comparison, the $P2p_{3/2}$ peak position for reference compounds in the NIST database shows binding energies of $Ni_3(PO_4)_2$ = 133.3 eV, Na_2HPO_3 = 132.9 eV, and NaH_2PO_2 = 132.6-132.9 eV [68]. On this basis, we assign the surface speciation upon air exposure to the formation of phosphorous oxide (likely a hypophosphite/phosphite), analogous to the behavior of nickel phosphides.[61,62] We note that removing this surface phosphor-oxide by etching prior to catalysis studies is necessary to obtain reproducible results with a total FE ~100% (see Fig. S1).

2.6. Atomic surface structure

Cu_3P is a high melting temperature (900°C), diamagnetic, non-conducting, inert solid (it does not react with water or air). Its standard enthalpy of formation relative to red P is $\Delta H_f^0 = -39.7 \pm 2.1$ kJ mol^{-1}. [69] It crystallizes in the hexagonal space group, $P6_3cm$, No. 185, which can be viewed as Cu_6P prisms with Cu atoms outside the faces of the prism. [70] Hence, P is coordinated to 11 Cu atoms, an unusually high number. [70] Cu_3P[00l] is known to be the preferred cleavage plane of bulk crystals in the absence of structure-directing ligands. [71] Literature studies predict that [002] and [l$\bar{l}$0]-facets are the most stable non-reconstructed facets, based on the highest atomic packing density at the surface using the Bravais-Friedel-Donnay-Harker (BFDH) crystal morphology algorithm. [72] Our HRTEM results show that during synthesis, the solvent TOP acts as a structure-directing agent selecting the Cu_3P[00l] surface. The Cu_3P[00l] facet may produce three different bulk terminations (prior to any surface reconstruction): Cu_4, Cu_3P_3, and Cu_6 (see SI Fig. S11). For Cu_3P[00I], the most phosphorous-rich termination is the Cu_3P[00I]-Cu_3P_3 (see Fig. 1B and SI Fig. S12). P rich terminations have been generally shown to be far more stable termination based on DFT calculations of the related Ni_xP_y compounds. [61,73,74] The Cu_3P_3 termination of the Cu_3P[00I] facet is also the most atomically dense, suggesting a high degree of saturated bonds, another sign of low surface energy (higher stability). The higher stability of P rich termination of both copper and nickel phosphides can be understood in terms of the bonding types described above: P enrichment relative to the bulk composition means more M-P (M = Ni/Cu) neighbors per unit area, hence lower surface energy. In the following mechanistic modeling, we use this prediction that Cu_3P_3 is the exposed termination of Cu_3P[00I] during CO_2RR.

2.7. Active site and reaction mechanism

CO_2RR mechanisms have been extensively studied on Cu metal and other mono-metallic surfaces. [37–39,75,76] However, much less is understood about the reaction on binary surfaces such as transition metal oxides and, in particular, transition metal phosphides. More is known about the CO_2RR mechanism on the nickel phosphides. [35]

CO_2RR on metallic Cu surfaces is postulated to proceed through *CO intermediates that combine on the surface to form the monoanion of ethene-1,2-dione, *O*CCO⁻, where * indicates a surface-bound atom. [39] This postulate comes from indirect evidence that $OCCO^-$ is known to be an isolable (stable) ion. [77] Such bidentate binding would require two adjacent surface atomic sites. Analogous to Cu, a debatable CO-based mechanism was recently proposed on a transition metal phosphide, FeP[2II] nanoarray catalyst, which produced methanol or ethanol in addition to H_2. [19] The author's DFT studies indicated that the Fe-Fe site distances are within a C-C coupling distance of two CO units for this compound. However, these calculations also showed a ~0.8 eV barrier to ethanol formation. This barrier is not in agreement with the experimental observation of the product formation at -0.2 V vs. RHE, casting serious doubt on the *a priori* assumption of a *CO mediated mechanism. Fig. 4A depicts the Cu_3P[00I]- Cu_3P_3 surface, where it can be seen that the (bulk) Cu-Cu distance of 4.11 Å is much greater than the 1.54 Å C-C bond distance of ethylene glycol (an approximate model for the $OCCO^-$ intermediate on Cu), thus precluding a Cu-centered *CO +*CO coupling reaction on this surface. Since only formate and no CO product are observed on Cu_3P NS/Cu, the CO_2RR mechanism must differ from that on metallic Cu. The absence of *CO intermediates is analogous to the mechanism proposed for CO_2RR on CuP_2, which yields 1-butanol. [46]

DFT calculations have suggested that all H-species bound on nickel phosphides are hydridic in nature (partial negative charge on H), making a hydride transfer mechanism feasible. [61,62] The notion that hydrides would be more reactive than surface-bound hydrogen atoms (or uncoupled H^+/e^- transfer steps) is supported by the Latimer-Frost diagram for CO_2 in Fig. S17. [78] The diagram shows that hydride transfer is strongly favored by nearly 1.37 eV compared to the sequential electron transfer (or concerted proton-electron transfer, for details, see SI).

Fig. 4B shows a side-view of the Cu_3P[00I]-Cu_3P_3 termination. The surface may be described as alternating rows of Cu and P atoms (with sub-surface layer Cu-P-tetrahedra), which together form CuP_3 trigonal pyramidal clusters (alternating triangles of CuP_3 (in blue in Fig. 4B)). Within the CuP_3 triangles, the Cu is distorted slightly out of the P-plane, alternating between sitting above and below the surface plane. The Cu-P distance is measured to be ~2.37 Å in the crystal structure. The Cu-Cu distance between Cu-P triangles distorted in the same direction out of the P-plane is 6.959 Å, while it is 4.111 Å between Cu atoms within alternately distorted sites. Fig. 4D shows a proposed mechanism on a CuP_3 trigonal pyramidal site present on the Cu_3P[00I]-Cu_3P_3 termination. This mechanism postulates a hydridic species (H^-) on the Cu_3P surface analogous to the related Ni_xP-compounds [61], and that predicted on Cu_3P [I$\bar{I}$0]. [72] There are three high symmetry surface sites on Cu_3P[00I]-Cu_3P_3; two CuP_3 trigonal pyramidals (dark and light blue, Fig. 4A) and one tetrahedral subsurface site (magenta and dark purple, Fig. 4A and B). The latter sub-surface site is coordinatively saturated and therefore unlikely to participate directly in the reaction mechanism. We also note that the surface P atoms are coordinated to 7 Cu atoms each; being coordinatively saturated, they are unlikely to participate in the binding of catalytic substrate. Since both the CuP_3 triangles populating this surface have coordinatively unsaturated Cu atoms, each is 3-coordinate and either slightly above the surface (dark blue) or slightly below the surface (light blue), the binding of protons (to form hydrides) or CO_2 can easily occur with minimal structural modification - a simple atomic displacement from trigonal pyramidal to tetrahedral. Hydride formation is expected to be quite facile for the Cu sites that lie above the surface.

Fig. 4C shows a qualitative atomic orbital diagram for the Cu(I) ion ($4s^1 3d^9$ electronic configuration) in the tetrahedral (subsurface) and trigonal pyramidal sites. It can be seen that the subsurface tetrahedral site has lower electron energy in the ground state compared to the surface trigonal pyramidal CuP_3, which has higher energy filled d-orbitals. By analogy, it is evident that monodentate binding of hydride, formate, or CO_2 at this active site to form a tetrahedral Cu(I) geometry gives a lower energy configuration. Thus, both energetics and stereochemical accessibility favors monodentate ligand binding at CuP_3.

As shown in Fig. 4D, our proposed mechanism starts with a 2-electron transfer upon proton binding to the trigonal pyramidal Cu(I), resulting in deformation to a tetrahedral geometry concurrent with hydride formation (H^-). This reaction should be driven by the change of electronic configuration to $4s^0 3d^{10}$, which is energetically favored in tetrahedral geometries, and by hybridization of H(1s) and Cu($3p_z$) orbitals to form the hydride bond (here denoted as H($1s^2$) for clarity). Importantly, this orbital assignment can also account for the observed absence of a reaction rate dependence on applied potential since these orbitals are isolated by energy and symmetry from other states near the Fermi level. In the following reaction step (see Fig. 4D), hydride formation at CuP_3 is the precursor for oxidative insertion of CO_2 into the Cu-H bond, resulting in the formation of a monodentate *formate species (analogous to the proposed mechanism on Ni_xP). [35] In the final step, the *formate intermediate is released by protonation, while the Cu(I) moves to its original trigonal pyramidal location, together with a return of the electronic configuration to $4s^1 3d^9$, leaving the surface open for subsequent catalytic turnover. In contrast to Cu_3P, the Ni_2P surface offers a slightly shorter distance Ni_3P-trigonal site and one fewer electron per Ni, which would readily allow stronger binding of bidentate formate. The proposed mono-dentate binding of formate to CuP_3 results in weaker binding and a lower population than on Ni_2P, thus explaining why hydride formation favors hydrogen production over CO_2 reduction on Cu_3P.

Finally, we note that there are literature reports of Cu_3P[I$\bar{I}$0] facet synthesis, [58] which, according to [79] also forms three terminations (see SI). These literature DFT calculations [79] predict that the Cu_3P[I$\bar{I}$0]-Cu_5P_2 termination is the most stable surface termination but undergoes a slight reconstruction to a more P-rich termination (see above). This termination exposes a distorted Cu_3 trigonal surface motif, consisting of two corner-sharing tetrahedral units and one corner-sharing trigonal planar CuP_x-unit (see SI Fig. S15 with the vertex P missing. This multi-Cu site has

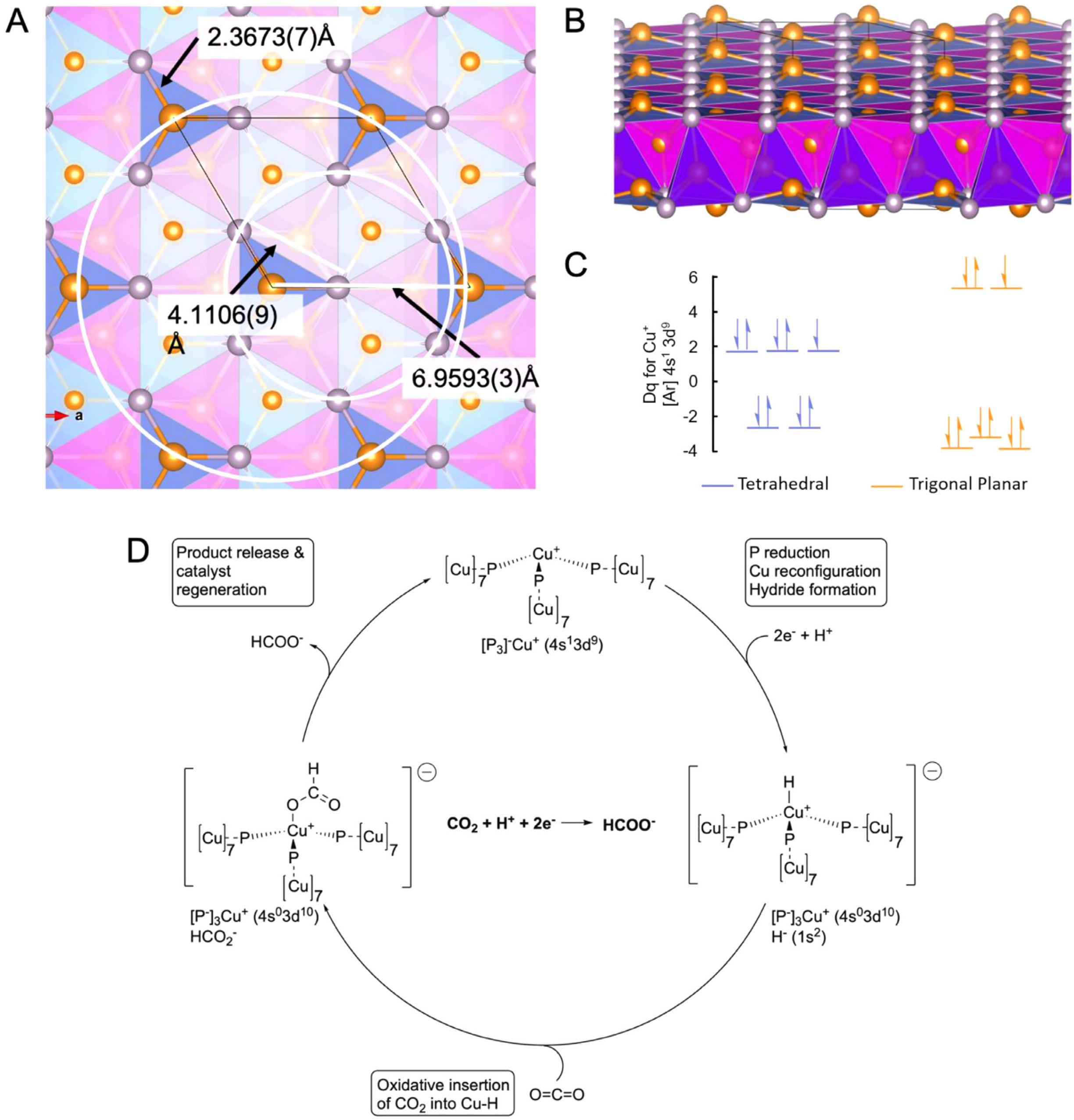

Fig. 4. (A): Top-view Cu_3P[00I]-Cu_3P_3 surface termination, showing the nearest Cu-Cu bond distance and Cu-P distance. Two types of trigonal CuP_3 sites: dark blue Cu is above surface P, and light blue Cu is below surface P; (B): Side view of the Cu_3P[00I]-Cu_3P_3 surface termination. (C0: Qualitative atomic orbital diagram of the trigonal pyramidal [CuP_3] units surface sites and the tetrahedral [CuP_4] units of the active site with monodentate ligand binding at the [CuP_3] unit. (D): Reaction mechanism of Cu_3P[00I]-Cu_3P_3 and schematic of active sites for formate.

clear similarities to the Ni_2P[00I]-Ni_2P_3 surface [74] — which consists of three corner-sharing tetrahedra with the vertex P missing at low applied potentials [49] — the most active for CO_2RR of the nickel phosphide compounds. [35] This Cu_3P[I$\bar{\text{I}}$0]-Cu_5P_2 surface would allow for C-C coupling since the Cu-Cu distances are only 2.57-2.71 Å. This surface has also been predicted by DFT calculations to have an H-binding energy of -12 and -36 meV on the two nonequivalent Cu_3 triangles formed by surface reconstruction.[72] Due to the near thermoneutral H bonding, these sites are expected to be highly labile and, consequently, could be more active for CO_2RR than the Cu_3P[00I]-Cu_3P_3 facet and Ni_2P[00I]-Ni_2P_3 (with H-binding energies of ~ -0.5 eV). Unfortunately, we note that the reported Cu_3P[I$\bar{\text{I}}$0] was grown on Ni foam and contains significant amounts of Ni, and when we attempted to apply the reported synthesis conditions to a Ni-free environment (using a Cu foam support), the resulting catalyst showed no preferential faceting. If an appropriate synthesis could be developed, the investigation of Cu_3P[I$\bar{\text{I}}$0] nanosheets could begin to investigate the importance of M_3 triangle sites as a potential active site for CO_2RR to $C_{n>1}$ products.

3. Conclusions

Among the several polymorphs of Cu_xP, each with slightly differing structures, we have produced a single-phase catalyst (P63cm space group) supported on metallic copper, which is well suited to electrochemical applications and mechanistic studies. Unlike most Cu, CuO_x, or copper oxide-derived CO_2RR electrocatalysts, which have low carbon selectivity that forms various C_1 and C_2 products, the Cu_3P NS/Cu catalyst exclusively forms formate at low overpotentials in competition with H_2 formation. Energetic considerations imply the CO_2RR mechanism to formate occurs via surface hydrides (not via one-electron pathways). Surface hydrides formed on Cu_3P strongly favor HER over CO_2RR in aqueous electrolytes, similar to Ni_3P, which contrasts with other Ni_xP_y compounds with higher P content (*e.g.* more hydride sites in closer proximity). [35,61,62] We have proposed a mechanism that explains this selectivity by considering the Cu_3P[00I] facet with Cu_3P_3-termination (predicted to be the most stable surface). We have given an electronic and structural argument explaining why the CuP_3 trigonal pyramidal sites form hydrides on copper sites that favor oxidative CO_2 insertion to formate with higher selectivity and comparable or higher TOF compared to both the Cu_2O and Cu benchmarks, which are known to yield C_1 and C_2 products at high overpotentials. Literature reports have correlated the latter activity to the Cu^+ sites retained on the surface under reductive conditions. Here, we have shown that the Cu^+ oxidation state alone is insufficient to achieve high CO_2RR activity and that close multi-copper sites are essential to produce C_2 or larger products.

Cu_3P NS/Cu exhibits a fairly negative open circuit potential of ~-100mV vs. RHE, which is more negative than what is observed on, *e.g.,* Ni_3P, $Ni_{12}P_5$, Ni_2P, and Ni_5P_4, [35] and which we argue is one manifestation of the different electronic structure that causes Cu_3P to be more prone to oxidation than the nickel-based phosphides. The presented data from Cu_3P NS/Cu allows us to deduce the following attributes needed to design a selective CO_2RR catalyst:

- Cu(I) alone is insufficient for an active CO_2RR site; a weakly bonded Cu-H (hydride) formation is the precursor to formate production.
- An active site that allows higher affinity (bidentate) bonding of the *formate intermediate is needed to out-compete HER (as in Ni_2P).
- To form C_2 and larger products, an additional requirement is a second hydridic site (P-H) within bonding distance ($<<$4.1Å) that enables reduction of *formate to *formaldehyde, which is a precursor to C-C coupling. [35]
- Coordinative stability of the Cu(I) species during catalytic turnover as occurs for Cu_3P provides long-term operational current stability resistant to reductive corrosion.
- According to this investigation, Cu_3P NS preferentially exposes a [00I] facet, which is proposed to form with a Cu_3P_3 termination.
- Under catalytic conditions, a surface hydride, Cu-H*, is active in both CO_2RR and especially HER catalysis.

Declaration of Competing Interest

The authors declare that they have no known competing financial interests or personal relationships that could have appeared to influence the work reported in this paper.

Credit authorship contribution statement

Anders B. Laursen: Conceptualization, Methodology, Formal analysis, Validation, Investigation, Data curation, Writing – original draft, Writing – review & editing. **Karin U.D. Calvinho:** Conceptualization, Methodology, Formal analysis, Validation, Investigation, Data curation, Writing – original draft, Writing – review & editing. **Timothy A. Goetjen:** Formal analysis, Investigation, Data curation, Writing – review & editing. **Kyra M.K. Yap:** Methodology, Validation, Investigation, Data curation, Writing – review & editing. **Shinjae Hwang:** Methodology, Formal analysis, Investigation, Data curation, Writing – original draft, Writing – review & editing. **Hongbin Yang:** Formal analysis, Investigation, Data curation, Writing – review & editing. **Eric Garfunkel:** Methodology, Formal analysis, Writing – review & editing, Supervision, Funding acquisition. **G. Charles Dismukes:** Conceptualization, Formal analysis, Writing – review & editing, Supervision, Project administration, Funding acquisition.

Acknowledgment

This work was supported by Rutgers TechAdvance through grant 205718. K.U.D.C. thanks the BASF Catalysis Division for a generous fellowship. Authors gratefully acknowledge funding from the NSF-CBET/EERE grant #CBET-1433492 and the continuation of DOE-EERE-FCTO grant #EE0008083. T.A.G. acknowledges support from the Aresty Undergraduate Research Institute and thanks the Rutgers Energy Institute for Summer support. G.C.D. thanks the Pray Family Foundation for their support.

Supplementary materials

Supplementary material associated with this article can be found, in the online version, at doi:10.1016/j.electacta.2021.138889.

References

[1] Y. Hori, Electrochemical CO_2 reduction on metal electrodes, in: C. Vayenas, R. White, M. Gamboa-Aldeco (Eds.), Mod. Asp. Electrochem., Springer, New York, 2008, pp. 89–189, doi:10.1007/978-0-387-49489-0_3.
[2] Y. Hori, S. Suzuki, Electrolytic reduction of carbon dioxide at mercury electrode in aqueous solution, Bull. Chem. Soc. Jpn. 55 (1982) 660–665, doi:10.1246/bcsj.55.660.
[3] B.a. Rosen, A. Salehi-Khojin, M.R. Thorson, W. Zhu, D.T. Whipple, P.J.a. Kenis, R.I. Masel, Ionic liquid-mediated selective conversion of CO_2 to CO at low overpotentials, Science (80-.) 334 (2011) 643–644, doi:10.1126/science.1209786.
[4] Y. Chen, C.W. Li, M.W. Kanan, Aqueous CO_2 reduction at very low overpotential on oxide-derived au nanoparticles, J. Am. Chem. Soc. 134 (2012) 19969–19972, doi:10.1021/ja309317u.
[5] C.W. Machan, S.A. Chabolla, J. Yin, M.K. Gilson, F.A. Tezcan, C.P. Kubiak, Supramolecular assembly promotes the electrocatalytic reduction of carbon dioxide by Re(I) bipyridine catalysts at a lower overpotential, J. Am. Chem. Soc. 136 (2014) 14598–14607, doi:10.1021/ja5085282.
[6] M. Peng, S. Ci, P. Shao, P. Cai, Z. Wen, Cu_3P/C nanocomposites for efficient electrocatalytic CO_2 reduction and Zn–CO_2 battery, J. Nanosci. Nanotechnol. 19 (2019) 3232–3236, doi:10.1166/jnn.2019.16589.
[7] K. Hara, A. Kudo, T. Sakata, Electrochemical reduction of carbon dioxide under high pressure on various electrodes in an aqueous electrolyte, J. Electroanal. Chem. 391 (1995) 141–147, doi:10.1016/0022-0728(95)03935-A.
[8] J. Wang, H. Wang, Z. Han, J. Han, Electrodeposited porous Pb electrode with improved electrocatalytic performance for the electroreduction of CO_2 to formic acid, Front. Chem. Sci. Eng. 9 (2015) 57–63, doi:10.1007/s11705-014-1444-8.
[9] C. Riplinger, M.D. Sampson, A.M. Ritzmann, C.P. Kubiak, E.A. Carter, Mechanistic contrasts between manganese and rhenium bipyridine electrocatalysts for the reduction of carbon dioxide, J. Am. Chem. Soc. 136 (2014) 16285–16298, doi:10.1021/ja508192y.
[10] A. Klinkova, P. De Luna, C.T. Dinh, O. Voznyy, E.M. Larin, E. Kumacheva, E.H. Sargent, Rational design of efficient palladium catalysts for electroreduction of carbon dioxide to formate, ACS Catal. 6 (2016) 8115–8120, doi:10.1021/acscatal.6b01719.
[11] S. Bontemps, L. Vendier, S. Sabo-Etienne, Ruthenium-catalyzed reduction of carbon dioxide to formaldehyde, J. Am. Chem. Soc. 136 (2014) 4419–4425, doi:10.1021/ja500708w.
[12] M. Rauch, Z. Strater, G. Parkin, Selective conversion of carbon dioxide to formaldehyde via a Bis(silyl)acetal: incorporation of isotopically labeled C1 moieties derived from carbon dioxide into organic molecules, J. Am. Chem. Soc. 141 (2019) 17754–17762, doi:10.1021/jacs.9b08342.
[13] K. Nakata, T. Ozaki, C. Terashima, A. Fujishima, Y. Einaga, High-yield electrochemical production of formaldehyde from CO_2 and seawater, Angew. Chem. Int. Ed. 53 (2014) 871–874, doi:10.1002/anie.201308657.
[14] T. Matsuo, H. Kawaguchi, From carbon dioxide to methane: homogeneous reduction of carbon dioxide with hydrosilanes catalyzed by zirconium−borane complexes, J. Am. Chem. Soc. 128 (2006) 12362–12363, doi:10.1021/ja0647250.
[15] H. Mistry, A.S. Varela, C.S. Bonifacio, I. Zegkinoglou, I. Sinev, Y.-W. Choi, K. Kisslinger, E.A. Stach, J.C. Yang, P. Strasser, B.R. Cuenya, Highly selective plasma-activated copper catalysts for carbon dioxide reduction to ethylene, Nat. Commun. 7 (2016) 12123, doi:10.1038/ncomms12123.

[16] D. Yang, Q. Zhu, C. Chen, H. Liu, Z. Liu, Z. Zhao, X. Zhang, S. Liu, B. Han, Selective electroreduction of carbon dioxide to methanol on copper selenide nanocatalysts, Nat. Commun. 10 (2019) 677, doi:10.1038/s41467-019-08653-9.
[17] X. Sun, L. Lu, Q. Zhu, C. Wu, D. Yang, C. Chen, B. Han, MoP nanoparticles supported on indium-doped porous carbon: outstanding catalysts for highly efficient CO_2 electroreduction, Angew. Chem. - Int. Ed. 57 (2018) 2427–2431, doi:10.1002/anie.201712221.
[18] S. Mou, T. Wu, J. Xie, Y. Zhang, L. Ji, H. Huang, T. Wang, Y. Luo, X. Xiong, B. Tang, X. Sun, Boron phosphide nanoparticles: a nonmetal catalyst for high-selectivity electrochemical reduction of CO_2 to CH_3OH, Adv. Mater. 31 (2019) 1903499, doi:10.1002/adma.201903499.
[19] L. Ji, L. Li, X. Ji, Y. Zhang, S. Mou, T. Wu, Q. Liu, B. Li, X. Zhu, Y. Luo, X. Shi, A.M. Asiri, X. Sun, Highly selective electrochemical reduction of CO_2 to alcohols on an FeP nanoarray, Angew. Chem. Int. Ed. 59 (2020) 758–762, doi:10.1002/anie.201912836.
[20] C.W. Li, J. Ciston, M.W. Kanan, Electroreduction of carbon monoxide to liquid fuel on oxide-derived nanocrystalline copper, Nature 508 (2014) 504–507, doi:10.1038/nature13249.
[21] A. Verdaguer-Casadevall, C.W. Li, T.P. Johansson, S.B. Scott, J.T. McKeown, M. Kumar, I.E.L. Stephens, M.W. Kanan, I. Chorkendorff, Probing the active surface sites for CO reduction on oxide-derived copper electrocatalysts, J. Am. Chem. Soc. 137 (2015) 9808–9811, doi:10.1021/jacs.5b06227.
[22] D. Ren, Y. Deng, A.D. Handoko, C.S. Chen, S. Malkhandi, B.S. Yeo, Selective electrochemical reduction of carbon dioxide to ethylene and ethanol on copper(I) oxide catalysts, ACS Catal. 5 (2015) 2814–2821, doi:10.1021/cs502128q.
[23] C.G. Morales-Guio, E.R. Cave, S.A. Nitopi, J.T. Feaster, L. Wang, K.P. Kuhl, A. Jackson, N.C. Johnson, D.N. Abram, T. Hatsukade, C. Hahn, T.F. Jaramillo, Improved CO_2 reduction activity towards C^{2+} alcohols on a tandem gold on copper electrocatalyst, Nat. Catal. 1 (2018) 764–771, doi:10.1038/s41929-018-0139-9.
[24] C.-T. Dinh, T. Burdyny, M.G. Kibria, A. Seifitokaldani, C.M. Gabardo, F.P. García de Arquer, A. Kiani, J.P. Edwards, P. De Luna, O.S. Bushuyev, C. Zou, R. Quintero-Bermudez, Y. Pang, D. Sinton, E.H. Sargent, CO_2 electroreduction to ethylene via hydroxide-mediated copper catalysis at an abrupt interface, Science (80-.) 360 (2018) 783–787, doi:10.1126/science.aas9100.
[25] H.S. Jeon, S. Kunze, F. Scholten, B.R. Cuenya, Prism-shaped Cu nanocatalysts for electrochemical CO_2 reduction to ethylene, ACS Catal. (2017) 531–535, doi:10.1021/acscatal.7b02959.
[26] Y. Hori, Electrochemical CO_2 reduction on metal electrodes, Mod. Asp. Electrochem. (2008) 89–189, doi:10.1007/978-0-387-49489-0_3.
[27] K.P. Kuhl, T. Hatsukade, E.R. Cave, D.N. Abram, J. Kibsgaard, T.F. Jaramillo, Electrocatalytic conversion of carbon dioxide to methane and methanol on transition metal surfaces, J. Am. Chem. Soc. 136 (2014) 14107–14113, doi:10.1021/ja505791r.
[28] A. Loiudice, P. Lobaccaro, E.A. Kamali, T. Thao, B.H. Huang, J.W. Ager, R. Buonsanti, Tailoring copper nanocrystals towards C_2 products in electrochemical CO_2 reduction, Angew. Chem. - Int. Ed. 55 (2016) 5789–5792, doi:10.1002/anie.201601582.
[29] S. Ma, M. Sadakiyo, M. Heima, R. Luo, R.T. Haasch, J.I. Gold, M. Yamauchi, P.J.A. Kenis, Electroreduction of carbon dioxide to hydrocarbons using bimetallic Cu–Pd catalysts with different mixing patterns, J. Am. Chem. Soc. 139 (2017) 47–50, doi:10.1021/jacs.6b10740.
[30] A. Eilert, F.S. Roberts, D. Friebel, A. Nilsson, Formation of copper catalysts for CO_2 reduction with high ethylene/methane product ratio investigated with in situ X-ray absorption spectroscopy, J. Phys. Chem. Lett. 7 (2016) 1466–1470, doi:10.1021/acs.jpclett.6b00367.
[31] F.P. García de Arquer, C.-T. Dinh, A. Ozden, J. Wicks, C. McCallum, A.R. Kirmani, D.-H. Nam, C. Gabardo, A. Seifitokaldani, X. Wang, Y.C. Li, F. Li, J. Edwards, L.J. Richter, S.J. Thorpe, D. Sinton, E.H. Sargent, CO_2 electrolysis to multicarbon products at activities greater than 1 A cm-2, Science 367 (2020) 661–666, doi:10.1126/science.aay4217.
[32] Y. Zhou, F. Che, M. Liu, C. Zou, Z. Liang, P. De Luna, H. Yuan, J. Li, Z. Wang, H. Xie, H. Li, P. Chen, E. Bladt, R. Quintero-Bermudez, T.-K. Sham, S. Bals, J. Hofkens, D. Sinton, G. Chen, E.H. Sargent, Dopant-induced electron localization drives CO_2 reduction to C_2 hydrocarbons, Nat. Chem. 10 (2018) 974–980, doi:10.1038/s41557-018-0092-x.
[33] C. Hahn, T. Hatsukade, Y.-G. Kim, A. Vailionis, J.H. Baricuatro, D.C. Higgins, S.A. Nitopi, M.P. Soriaga, T.F. Jaramillo, Engineering Cu surfaces for the electrocatalytic conversion of CO_2 : controlling selectivity toward oxygenates and hydrocarbons, Proc. Natl. Acad. Sci. 114 (2017) 5918–5923, doi:10.1073/pnas.1618935114.
[34] Z. Han, R. Kortlever, H.-Y. Chen, J.C. Peters, T. Agapie, CO_2 reduction selective for $C_{\geq 2}$ products on polycrystalline copper with N-Substituted pyridinium additives, ACS Cent. Sci. 3 (2017) 853–859, doi:10.1021/acscentsci.7b00180.
[35] K.U.D. Calvinho, A.B. Laursen, K.M.K. Yap, T.A. Goetjen, S. Hwang, N. Murali, B. Mejia-Sosa, A. Lubarski, K.M. Teeluck, E.S. Hall, E. Garfunkel, M. Greenblatt, G.C. Dismukes, Selective CO_2 reduction to C_3 and C_4 oxyhydrocarbons on nickel phosphides at overpotentials as low as 10 mV, Energy Environ. Sci. 11 (2018) 2550–2559, doi:10.1039/C8EE00936H.
[36] P. Gao, S. Li, X. Bu, S. Dang, Z. Liu, H. Wang, L. Zhong, M. Qiu, C. Yang, J. Cai, W. Wei, Y. Sun, Direct conversion of CO_2 into liquid fuels with high selectivity over a bifunctional catalyst, Nat. Chem. 9 (2017) 1019–1024, doi:10.1038/nchem.2794.
[37] A.A. Peterson, F. Abild-Pedersen, F. Studt, J. Rossmeisl, J.K. Nørskov, How copper catalyzes the electroreduction of carbon dioxide into hydrocarbon fuels, Energy Environ. Sci. 3 (2010) 1311, doi:10.1039/c0ee00071j.
[38] A.A. Peterson, J.K. Nørskov, Activity descriptors for CO_2 electroreduction to methane on transition-metal catalysts, J. Phys. Chem. Lett. 3 (2012) 251–258, doi:10.1021/jz201461p.
[39] R. Kortlever, J. Shen, K.J.P. Schouten, F. Calle-Vallejo, M.T.M. Koper, Catalysts and reaction pathways for the electrochemical reduction of carbon dioxide, J. Phys. Chem. Lett. 6 (2015) 4073–4082, doi:10.1021/acs.jpclett.5b01559.
[40] J. Kim, W. Choi, J.W. Park, C. Kim, M. Kim, H. Song, Branched copper oxide nanoparticles induce highly selective ethylene production by electrochemical carbon dioxide reduction, J. Am. Chem. Soc. 141 (2019) 6986–6994, doi:10.1021/jacs.9b00911.
[41] R. Kas, R. Kortlever, A. Milbrat, M.T.M. Koper, G. Mul, J. Baltrusaitis, Electrochemical CO_2 reduction on Cu_2O-derived copper nanoparticles: controlling the catalytic selectivity of hydrocarbons, Phys. Chem. Chem. Phys. 16 (2014) 12194–12201, doi:10.1039/c4cp01520g.
[42] J.B. Varley, H.A. Hansen, N.L. Ammitzbøll, L.C. Grabow, A.A. Peterson, J. Rossmeisl, J.K. Nørskov, Ni-Fe-S cubanes in CO_2 reduction electrocatalysis: a DFT study, ACS Catal. 3 (2013) 2640–2643, doi:10.1021/cs4005419.
[43] P. Amara, J.-M. Mouesca, A. Volbeda, J.C. Fontecilla-Camps, Carbon monoxide dehydrogenase reaction mechanism: a likely case of abnormal CO_2 insertion to a Ni−H^- bond, Inorg. Chem. 50 (2011) 1868–1878, doi:10.1021/ic102304m.
[44] C. Drennan, T. Doukov, S. Ragsdale, The metalloclusters of carbon monoxide dehydrogenase/acetyl-CoA synthase: a story in pictures, JBIC J. Biol. Inorg. Chem. 9 (2004) 511–515, doi:10.1007/s00775-004-0563-y.
[45] T. Mizuno, A.H. Weiss, Synthesis and utilization of Formose sugars, in: R.S. Tipson, D. Horton (Eds.), Advances in Carbohydrate Chemistry and Biochemistry, 1974.
[46] M. Choi, S. Bong, J. Won Kim, J. Lee, Formation of 1-butanol from CO_2 without *CO dimerization on a phosphorus-rich copper cathode, ACS Energy Lett. 6 (2021) 2090–2095, doi:10.1021/acsenergylett.1c00723.
[47] V.E. Bazhenov, I.N. Pashkov, M.V. Pikunov, Investigating crystallization processes while brazing copper by copper-phosphorus brazing alloy with the purpose of controlling the structure of the brased seam, Russ. J. Non-Ferrous Met. 54 (2013) 43–47, doi:10.3103/S1067821213010021.
[48] C.A. Downes, N.J. Libretto, A.E. Harman-Ware, R.M. Happs, D.A. Ruddy, F.G. Baddour, J.R. Ferrell III, S.E. Habas, J.A. Schaidle, Electrocatalytic CO_2 reduction over Cu_3P nanoparticles generated via a molecular precursor route, ACS Appl. Energy Mater. (2020), doi:10.1021/acsaem.0c01360.
[49] R.B. Wexler, J.M.P. Martirez, A.M. Rappe, Active role of phosphorus in the hydrogen evolving activity of nickel phosphide (0001) surfaces, ACS Catal. 7 (2017) 7718–7725, doi:10.1021/acscatal.7b02761.
[50] A. Alherz, C.H. Lim, Y.C. Kuo, P. Lehman, J. Cha, J.T. Hynes, C.B. Musgrave, Renewable hydride donors for the catalytic reduction of CO_2: a thermodynamic and kinetic study, J. Phys. Chem. B 122 (2018) 10179–10189, doi:10.1021/acs.jpcb.8b08536.
[51] E.S. Wiedner, M.B. Chambers, C.L. Pitman, R.M. Bullock, A.J.M. Miller, A.M. Appel, Thermodynamic hydricity of transition metal hydrides, Chem. Rev. 116 (2016) 8655–8692, doi:10.1021/acs.chemrev.6b00168.
[52] H. Fong, J.C. Peters, Hydricity of an Fe–H species and catalytic CO_2 hydrogenation, Inorg. Chem. (2014) 150128084746000, doi:10.1021/ic502508p.
[53] A. Eilert, F. Cavalca, F.S. Roberts, J. Osterwalder, C. Liu, M. Favaro, E.J. Crumlin, H. Ogasawara, D. Friebel, L.G.M. Pettersson, A. Nilsson, Subsurface oxygen in oxide-derived copper electrocatalysts for carbon dioxide reduction, J. Phys. Chem. Lett. 8 (2017) 285–290, doi:10.1021/acs.jpclett.6b02273.
[54] R.B. Wexler, J.M.P. Martirez, A.M. Rappe, Chemical pressure-driven enhancement of the hydrogen evolving activity of Ni_2P from nonmetal surface doping interpreted via machine learning, J. Am. Chem. Soc. 140 (2018) 4678–4683, doi:10.1021/jacs.8b00947.
[55] F.H. Saadi, A.I. Carim, E. Verlage, J.C. Hemminger, N.S. Lewis, M.P. Soriaga, CoP as an acid-stable active electrocatalyst for the hydrogen-evolution reaction: Electrochemical synthesis, interfacial characterization and performance evaluation, J. Phys. Chem. C 118 (2014) 29294–29300, doi:10.1021/jp5054452.
[56] Y. Hori, A. Murata, R. Takahashi, Formation of hydrocarbons in the electrochemical reduction of carbon dioxide at a copper electrode in aqueous solution, J. Chem. Soc. Faraday Trans. 1 Phys. Chem. Condens. Phases 85 (1989) 2309, doi:10.1039/f19898502309.
[57] C.W. Li, M.W. Kanan, CO_2 reduction at low overpotential on Cu electrodes resulting from the reduction of thick Cu_2O films, J. Am. Chem. Soc. 134 (2012) 7231–7234, doi:10.1021/ja3010978.
[58] A. Han, H. Zhang, R. Yuan, H. Ji, P. Du, Crystalline copper phosphide nanosheets as an efficient janus catalyst for overall water splitting, ACS Appl. Mater. Interfaces 9 (2017) 2240–2248, doi:10.1021/acsami.6b10983.
[59] J. Kibsgaard, C. Tsai, K. Chan, J.D. Benck, J.K. Nørskov, F. Abild-Pedersen, T.F. Jaramillo, Designing an improved transition metal phosphide catalyst for hydrogen evolution using experimental and theoretical trends, Energy Environ. Sci. 8 (2015) 3022–3029, doi:10.1039/C5EE02179K.
[60] A.B. Laursen, K.R. Patraju, M.J. Whitaker, M. Retuerto, T. Sarkar, N. Yao, K.V. Ramanujachary, M. Greenblatt, G.C. Dismukes, Nanocrystalline Ni_5P_4: a hydrogen evolution electrocatalyst of exceptional efficiency in both alkaline and acidic media, Energy Environ. Sci. 8 (2015) 1027–1034, doi:10.1039/C4EE02940B.
[61] A.B. Laursen, R.B. Wexler, M.J. Whitaker, E.J. Izett, K.U.D. Calvinho, S. Hwang, R. Rucker, H. Wang, J. Li, E. Garfunkel, M. Greenblatt, A.M. Rappe, G.C. Dismukes, Climbing the volcano of electrocatalytic activity while avoiding catalyst corrosion: Ni_3P, a hydrogen evolution electrocatalyst stable in both acid and alkali, ACS Catal. 8 (2018) 4408–4419, doi:10.1021/acscatal.7b04466.
[62] A.B. Laursen, K.R. Patraju, M.J. Whitaker, M. Retuerto, T. Sarkar, N. Yao, K.V. Ramanujachary, M. Greenblatt, G.C. Dismukes, Nanocrystalline Ni_5P_4: a hydrogen

evolution electrocatalyst of exceptional efficiency in both alkaline and acidic media, Energy Environ. Sci. 8 (2015) 1027–1034, doi:10.1039/C4EE02940B.
[63] H. Yin, S. Zhao, K. Zhao, A. Muqsit, H. Tang, L. Chang, H. Zhao, Y. Gao, Z. Tang, Ultrathin platinum nanowires grown on single-layered nickel hydroxide with high hydrogen evolution activity, Nat. Commun. 6 (2015) 6430, doi:10.1038/ncomms7430.
[64] R. Kortlever, I. Peters, S. Koper, M.T.M. Koper, Electrochemical CO_2 reduction to formic acid at low overpotential and with high faradaic efficiency on carbon-supported bimetallic Pd–Pt nanoparticles, ACS Catal. 5 (2015) 3916–3923, doi:10.1021/acscatal.5b00602.
[65] A.W. Kahsay, K.B. Ibrahim, M.-C. Tsai, M.K. Birhanu, S.A. Chala, W.-N. Su, B.-J. Hwang, Selective and low overpotential electrochemical CO_2 reduction to formate on CuS decorated CuO heterostructure, Catal. Lett. 149 (2019) 860–869, doi:10.1007/s10562-019-02657-2.
[66] S. Zhang, P. Kang, T.J. Meyer, Nanostructured tin catalysts for selective electrochemical reduction of carbon dioxide to formate, J. Am. Chem. Soc. 136 (2014) 1734–1737, doi:10.1021/ja4113885.
[67] Thermo Scientific XPS, (2013). https://xpssimplified.com/elements/copper.php#appnotes.
[68] A.V. Naumkin, A. Kraut-Vass, S.W. Gaarenstroom, C.J. Powell, NIST X-ray photoelectron spectroscopy database, Natl. Inst. Stand. Technol. (2012).
[69] S. Boone, O.J. Kleppa, Determination of the standard enthalpy of formation of Cu_3P by direct-combination drop calorimetry, Thermochim. Acta 202 (1992) 113–119, doi:10.1016/0040-6031(92)85157-Q.
[70] O. Olofsson, L. Holmlund, N. Ingri, M.J. Tricker, S. Svensson, The crystal structure of Cu_3P, Acta Chem. Scand. 26 (1972) 2777–2787, doi:10.3891/acta.chem.scand.26-2777.
[71] Steel Data, Copper phosphide - Cu3P, Etchants Database. (n.d.). http://www.steeldata.info/etch/demo/help/compounds/41.html (accessed April 22, 2020).
[72] Z. Zhang, G. Yu, H. Li, J. Liu, X. Huang, W. Chen, Theoretical insights into the effective hydrogen evolution on Cu3P and its evident improvement by surface-doped Ni atoms, Phys. Chem. Chem. Phys. 20 (2018) 10407–10417, doi:10.1039/C8CP00644J.
[73] D. Fuks, D. Vingurt, M.V. Landau, M. Herskowitz, Density functional theory study of sulfur adsorption at the (001) surface of metal-rich nickel phosphides: effect of the Ni/P ratio, J. Phys. Chem. C 114 (2010) 13313–13321, doi:10.1021/jp1031306.
[74] R.B. Wexler, J.M.P. Martirez, A.M. Rappe, Stable phosphorus-enriched (0001) surfaces of nickel phosphides, Chem. Mater. 28 (2016) 5365–5372, doi:10.1021/acs.chemmater.6b01437.
[75] Y. Hori, O. Koga, A. Aramata, M. Enyo, Infrared spectroscopic observation of adsorbed carbon dioxide intermediately formed in the electrochemical reduction of carbon dioxide at a nickel electrode, Bull. Chem. Soc. Jpn. 65 (1992) 3008–3010, doi:10.1246/bcsj.65.3008.
[76] A. Bagger, W. Ju, A.S. Varela, P. Strasser, J. Rossmeisl, Electrochemical CO_2 reduction: a classification problem, ChemPhysChem 18 (2017) 3266–3273, doi:10.1002/cphc.201700736.
[77] J.R. Thomas, B.J. DeLeeuw, P. O'Leary, H.F. Schaefer III, B.J. Duke, B. O'Leary, The ethylenedione anion: elucidation of the intricate potential energy hypersurface, J. Chem. Phys. 102 (1995) 6525–6536.
[78] J. Schneider, H. Jia, J.T. Muckerman, E. Fujita, Thermodynamics and kinetics of CO_2, CO, and H^+ binding to the metal centre of CO_2 reduction catalysts, Chem. Soc. Rev. 41 (2012) 2036–2051, doi:10.1039/c1cs15278e.
[79] Z. Zhang, G. Yu, H. Li, J. Liu, X. Huang, W. Chen, Theoretical insights into the effective hydrogen evolution on Cu_3P and its evident improvement by surface-doped Ni atoms, Phys. Chem. Chem. Phys. 20 (2018) 10407–10417, doi:10.1039/C8CP00644J.